C. R. Mecanique 347 (2019) 930–943

Contents lists available at ScienceDirect

Comptes Rendus Mecanique

www.sciencedirect.com

# Influence of geometry on stress state in bulk characterization tests

Sonda Moakhar, Hamdi Hentati *, Maher Barkallah, Jamel Louati, Mohamed Haddar

*Research Laboratory of Mechanics, Modeling and Manufacturing (LA2MP), National Engineering School of Sfax, University of Sfax, Tunisia*

ARTICLE INFO

*Article history:*
Received 7 August 2019
Accepted 6 October 2019
Available online 13 November 2019

*Keywords:*
Characterization tests
Bulk metalworking
Triaxiality
Lode parameter

ABSTRACT

This paper is concerned with the selection of the geometries of test specimens for bulk metal characterization tests. Simulations of characterization tests on cylindrical, notched, and shear specimens were conducted to allow for the analysis of stress state evolution during the tests and to evidence the impact of geometry on stress state. Both stress triaxiality and Lode parameter were considered for selecting representative specimens. Three choice criterions were regarded: the diversification of stress states as well as the constancy and the nearness of stress state indicators to the theoretical values along the deformation.

© 2019 Académie des sciences. Published by Elsevier Masson SAS. All rights reserved.

## 1. Introduction

In recent years, many researches have been dedicated to material models in order to predict correctly the material behavior under different stress states. The accuracy of these models is crucial for the success of the simulation of bulk metalworking processes. Numerical analysis of these processes help reduce the duration and the cost of development phase. Metals behavior consist in elastic-plastic modelling and damage modelling. The calibration of elastic-plastic models is generally based on simple tension or compression tests. The calibration of damage models is based on failure characteristic tests. Aside from the choice of the damage model, the selection of the characterization tests is very important and should reproduce the stress states involved in the studied metalworking processes. Hereby, the geometry of the tests specimens plays a determining role in the resulting stress state in the fracture zone. While numerous researches focused on the determination of the fracture limit in sheet metalworking processes such as [1–3], only few publications were found on the fracture limit in bulk metalworking processes. Fracture is considered as a defect in some processes like external and internal cracking in extrusion or open die forging. In this case, fracture modeling serves as a tool to numerically regulate the process and to avoid defects. In other processes like shearing and sawing, fracture is desired and has to be appropriately modeled in order to ameliorate the quality of the final product. A number of experimental works have found that ductility in plain strain specimens is less than in axisymmetric specimens [4]. Furthermore, failure mechanisms in bulk metal forming are different from the ones in sheet metal forming [5]. Consequently, the characterization of bulk metal behavior should be based on tests with bulk metal specimens.

* Corresponding author.
*E-mail address:* Hamdi.hentati@yahoo.fr (H. Hentati).

https://doi.org/10.1016/j.crme.2019.10.003
1631-0721/© 2019 Académie des sciences. Published by Elsevier Masson SAS. All rights reserved.

The interaction between stress state and ductile failure mechanisms was proven in the early 1960s in the experimental work of Bridgman [6]. Material characteristics such as microstructure, inclusion content, morphology, and grain size, in addition to conditions between tool and die, have also an influence on ductility [7].

Bulk metalworking processes are characterized by a dominant compressive stress state with manifestation of tensile stresses in specific locations [7]. The dominating stress state in bulk metal forming processes like rolling, extrusion, and forging is compression [8]. In wire drawing process, a uniaxial tension is additionally established in the deformation zone. Moreover, shear strains induce internal shear cracking [9]. Thus, the characterization tests should be representative of a wide range of stress states to allow an accurate prediction of failure during bulk metalworking processes.

The question then arises of how to represent the stress states with measurable variables. The most known stress state indicator is stress triaxiality. It is calculated from the first and second stress invariants. Its central role in the ductile fracture mechanism was firstly demonstrated by Rice and Tracy [10]. The Bao–Wierzbicki damage model is based on the computation of the integral of triaxiality over plastic deformation to predict material failure [11]. This model has found a good application in the simulation of tensile tests on notched and unnotched specimens [12]. Oyane's damage model relates the volume of pores during deformation to an integral function of triaxiality [13]. The suitability of this model in predicting ductile damage in bulk metal processes was proven by many authors [14,15]. The Johnson–Cook damage model calculates fracture strains as a function of triaxiality, strain rate, and temperature [16]. This model is commonly used in the simulation of machining processes, ballistic perforation and other metal-forming processes involving high strains, strain rates, and temperatures [17–20].

Nevertheless, recent studies demonstrated that the third deviatoric invariant is worth to be considered in failure modeling, especially when a low level of triaxiality is encountered [4,21]. As a result, they suggested combining the triaxiality and the Lode parameter as an adequate stress state evaluation in the prediction of failure. The fracture locus is thus represented as a three-dimensional function in the space of equivalent strain to fracture, triaxiality, and Lode parameter (or Lode angle parameter). This method was adopted by many studies, since it helps better illustrate three-dimensional fracture mechanisms [22].

Characterization tests allow us to analyze the failure mechanisms and to eventually provide a fracture locus for a specific material. The classical bulk tests are tensile tests on round bars like in [23]. In order to cover a wide range of stress states, Bao and Wierzbickie [11] have considered compression, tension, and shear tests on axisymmetric and plate specimens. Erice and Gálvez [24] have combined quasi-static tensile tests on axisymmetric and plane specimens with dynamic tests on axisymmetric specimens. The fracture mechanisms in bulk metal forming result from two crack separation modes: tensile stresses and out-of-plane shear stresses [25]. An appropriate fracture locus for bulk metal is based on bulk specimens like cylindrical, tapered, flanged, and ring specimens [5]. Furthermore, shear failure properties should be characterized with shear and shear dominant test specimens. Meyer and Halle [26] have investigated typical shear tests to measure flow and failure behavior at shear and shear-dominated stress states.

Plasticity modeling is also of great interest in the numerical analysis of metalworking processes. It describes material behavior in the elastic-plastic zone. One of the most known models is the Johnson–Cook constitutive model [27], which allows one to include the effect of work hardening, strain rate hardening, and thermal softening in the calculation of the flow stress. This model was used in the simulation of many processes like machining, forging, and ballistic perforation [28–30].

The material studied in this work is A1045 steel. The dependency of its flow stress on temperature, plastic strain, and strain has been proven [31]. Many authors have calibrated the Johnson–Cook model appropriately for A1045. For this purpose, Jaspers and Dautzenberg [32], among others, have used split Hopkinson pressure bar tests (SHPB) at elevated temperatures and high strain rates. In the current study, the already calibrated Johnson–Cook plasticity equation is utilized in the numerical simulations.

This study was designed to evaluate stress state evolution in bulk metal characterization tests. Only bulk specimens were considered. In order to analyze the influence of the specimens' geometries on the stress state, four types of characterization tests were modeled with ABAQUS/Explicit: upsetting tests, smooth round bars for traction, notched round bars for traction, and shear tests. In every test type, many specimen variants were compared. The choice of the best specimen geometry was based on the observation of triaxiality and the Lode parameter during deformation. The specimens having the most stable and accurate stress state variables were retained.

## 2. Stress state variables

### 2.1. Stress triaxiality

Stress triaxiality, or triaxiality ($\eta$), is a dimensionless ratio expressed with the following equation:

$$\eta = \frac{\sigma_{\mathrm{m}}}{\sigma_{\mathrm{eq}}} \tag{1}$$

where $\sigma_{\mathrm{m}}$ is the hydrostatic stress:

$$\sigma_{\mathrm{m}} = \frac{I_1}{3} = \frac{\sigma_1 + \sigma_2 + \sigma_3}{3} \tag{2}$$

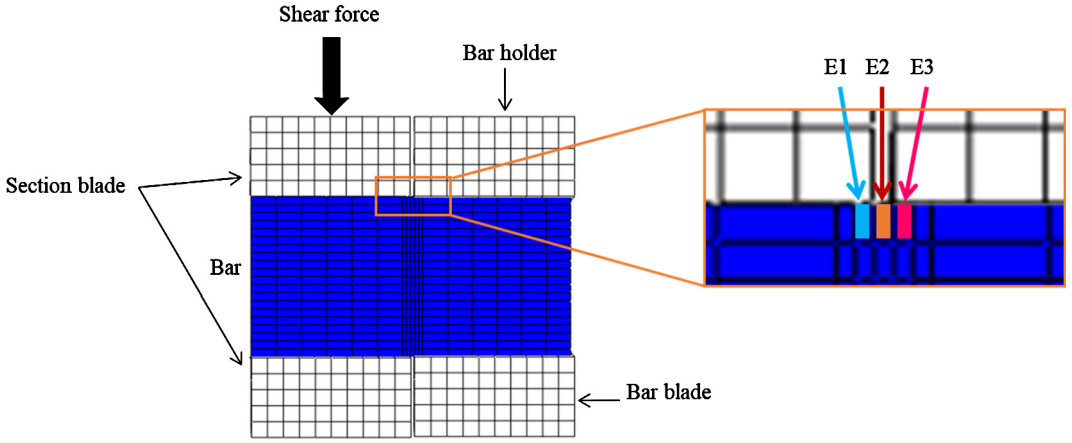


**Fig. 1.** Shearing model and selected elements for stress state analysis.

In addition, $\sigma_{eq}$ is the von Mises equivalent stress:

$$\sigma_{eq} = \sqrt{\frac{1}{2}[(\sigma_1 - \sigma_2)^2 + (\sigma_2 - \sigma_3)^2 + (\sigma_3 - \sigma_1)^2} = \sqrt{3J_2} \tag{3}$$

$\sigma_1$, $\sigma_2$, and $\sigma_3$ are the principal stresses with the assumption: $\sigma_1 \geq \sigma_2 \geq \sigma_3$.

From Eqs. (1)–(3), triaxiality can be expressed as a function of the first and second stress invariants $I_1$ and $J_2$, as follows:

$$\eta = \frac{I_1}{3\sqrt{3J_2}} = \frac{\sigma_1 + \sigma_2 + \sigma_3}{3\sqrt{\frac{1}{2}[(\sigma_1 - \sigma_2)^2 + (\sigma_2 - \sigma_3)^2 + (\sigma_3 - \sigma_1)^2}} \tag{4}$$

### 2.2. Lode parameter

Lode [33] had the idea to characterize the stress state in thin wall metal tubes with the variable $\mu$, which is calculated in terms of the principal stresses as follows:

$$\mu = \frac{2\sigma_2 - \sigma_1 - \sigma_3}{\sigma_1 - \sigma_3}; \quad -1 \leq \mu \leq 1 \tag{5}$$

This parameter $\mu$ is closely related to the Lode angle, which has an influence on the shape of the yield surface [34]. The Lode angle ($\theta$) is related to the second and third deviatoric invariants ($J_2$ and $J_3$) according to the following equation [35]:

$$\cos 3\theta = \frac{3\sqrt{3}}{2}\frac{J_3}{J_2^{1.5}}; \quad 0 \leq \theta \leq \frac{\pi}{3} \tag{6}$$

where $J_3$ is the determinant of the deviatoric stress tensor. While all of the three stress invariants are employed to calculate the triaxiality and the Lode angle, any stress state can be mathematically written in terms of these two variables, as follows [36]:

$$\frac{3}{2\sigma_{eq}}\begin{pmatrix}\sigma_1\\ \sigma_2\\ \sigma_3\end{pmatrix} = \frac{3}{2}\eta\begin{pmatrix}1\\ 1\\ 1\end{pmatrix} + \frac{2}{\sqrt{3}}\sqrt{J_2}\begin{pmatrix}-\cos(\theta+60)\\ -\cos(\theta-60)\\ \cos\theta\end{pmatrix} \tag{7}$$

### 2.3. Examination of stress state variables in shearing simulation

Moakhar et al. [37] have constructed a three-dimensional finite element model of bar shearing. They proved the existence of different stress states in the sheared bar during the deformation before the total rupture. Shearing tool consists of a moving section blade, a bar blade, and a bar holder. These are modeled as rigid bodies (Fig. 1). The material constituting the bar was aluminum alloy AW6082, and has been modeled using an elastic-plastic formulation and damage prediction calibrated with Hooputra's damage model. The observation of the authors was limited to the evolution of stress triaxiality. In this work, a general examination of the evolution of the stress state during the bar shearing process was conducted. For this purpose, the triaxialities and Lode parameters of three representative elements in the shear zone were examined.

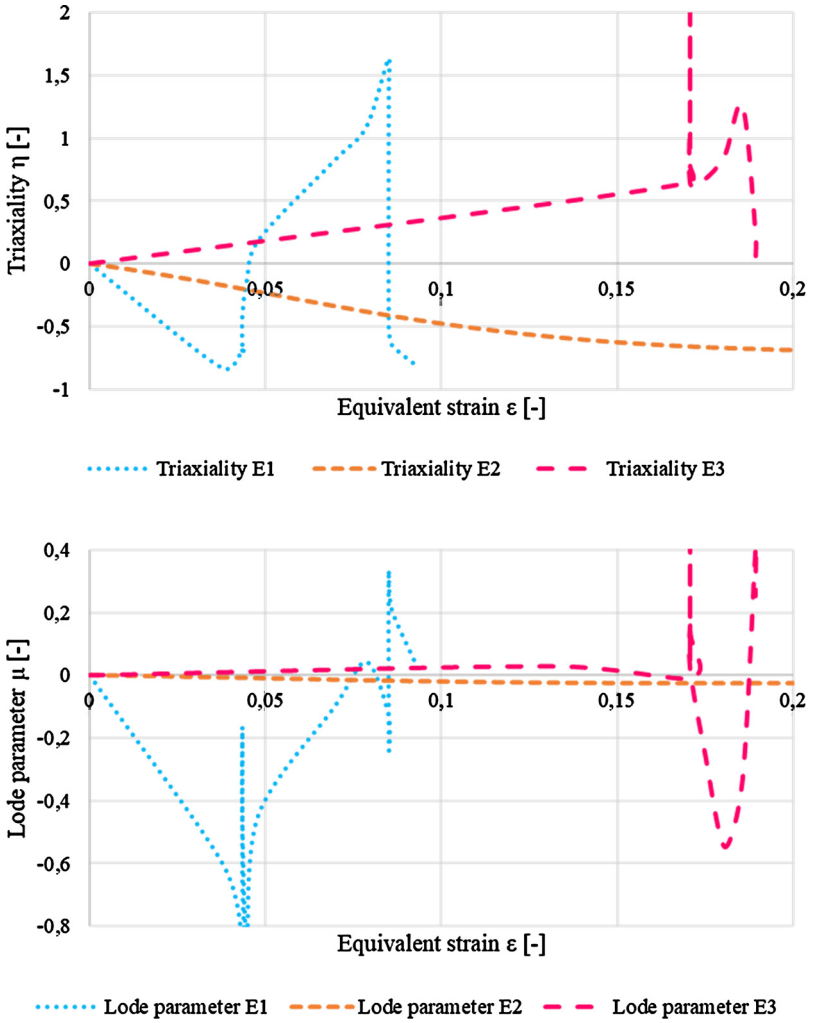


**Fig. 2.** Evolution of triaxiality and of the Lode parameter in E1, E2, and E3.

Element E1 was located in the contact surface between the bar and the section blade, element E2 was picked from the middle of the shear zone, and element E3 was situated at the contact surface between the bar and the bar holder.

Fig. 2 shows the evolution of triaxiality and of the Lode parameter along the deformation at every selected element. Element E1 has a positive triaxiality and a negative Lode parameter, which evidences a dominating tension stress state. In the case of element E2, triaxiality is negative and the Lode parameter is close to zero, indicating a dominance of the shear stress state. The third element E3 has a positive triaxiality and a Lode parameter close to zero, as well as a combined positive–negative peak at a deformation comprised between 0.15 and 0.2. Thanks to this preliminary simulation, the existence of various stress states in the deformed metal was proven.

## 3. Numerical procedure

The aim of this numerical study is to choose representative specimens covering a large range of triaxiality and Lode parameters under the restraints of stability of these measures through the deformation and the closeness to the analytical values. For this reason, four types of characterization tests were simulated with ABAQUS/Explicit: compression of cylindrical specimens, traction of smooth round bars, traction of notched round bars, and shear tests. The geometries of the specimens are presented in the next section.

### *3.1. Global mechanical formulation*

The modeled test specimens are considered as three-dimensional bodies subjected to surface and body forces [38]. Depending on the geometry of the body, the applied loads, the boundary conditions, and the behavior law of the material, the FEM calculation determines the displacement vector $u(X,t)$ of all elements and at every time. $X$ is the vector representing

the initial space coordinates. A static problem is described by the momentum conservation equation (Eq. (8)), the material constitutive law, the friction conditions on $S_\sigma$ (Eq. (9)) and the boundary conditions on $S_T$ (Eq. (10)).

$$\nabla\sigma + F_v = 0 \tag{8}$$

where $\sigma$ is Cauchy stress tensor, $\nabla$ is the gradient operator, $F_v$ is the body force vector applied on the surface $S_F$.

$$\tau_f = \mathrm{Min}\left(\mu_C \sigma_N, m\frac{\sigma_y}{\sqrt{3}}\right) \tag{9}$$

where $\tau_f$ is the friction shear stress, $\mu_C$ is the Coulomb friction coefficient, $\sigma_N$ is the contact normal stress, $m$ is Tresca's friction factor and $\sigma_y$ is the yield stress; $F_f$ is the he contact force applied on the surface $S_\sigma$.

The traction boundary conditions on $S_T$ are defined by the following equation:

$$\sigma \cdot n = T \tag{10}$$

where $n$ is an outward unit vector, $T$ is the surface traction applied on the surface $S_T$. The body is assumed to have the volume $V$ bounded with the surface $S$:

$$S = S_F \cup S_\sigma \cup S_T \tag{11}$$

The variational equation is obtained from the principle of virtual work, which claims that for all virtual displacement $\delta u$, the sum of all mechanical works of a system vanishes. After applying the Gauss divergence theorem, the weak form of the equilibrium can be written as follows:

$$-\int_V \nabla\sigma\,\delta\dot{u}\,\mathrm{d}V + \int_{S_F} F_v\delta u\,\mathrm{d}V + \int_{S_\sigma} F_f\delta u\,\mathrm{d}S + \int_{S_T} T\delta u\,\mathrm{d}S = 0 \tag{12}$$

### 3.2. Finite-element discretization

Three-dimensional models were constructed so as to benefit from symmetry conditions. In compression and traction tests, eighth models were designed. In the axisymmetric shear tests, quarter models were used. The shear specimen S4 has only one symmetry plane and its depth is 10 mm. In all tests, the top side is subjected to a simple tension or compression with a constant velocity of 10 mm/s. The dies were modeled with rigid contact elements in compression and shear tests.

From the outputs of the simulations, the stress state is observed along the deformation. The Lode parameter and triaxiality are calculated based on the central elements of the rupture zone to evaluate the stress state at the point where the rupture starts. The analytical values of these parameters can be calculated after understanding the respective Mohr circles to the main stress states.

### 3.3. Sensitivity study and meshing

The utilized element is the quadrilateral element with linear interpolation functions and reduced integration (C3D8R). The reduced integration technique permits to avoid locking problems due to plastic incompressibility [39]. A study on the sensibility to the mesh size was established for every test in order to distinguish the maximal mesh size that allows the stability of the studied triaxiality curve. Three mesh sizes were applied in the rupture zone: 0.3, 0.4, and 0.5 mm. From the comparison of the obtained triaxiality evolution (Fig. 3), it was obvious that, from 0.4 mm, the computed results are not affected by changing the mesh size.

In order to reduce the computational cost, a fine meshing is applied only in the rupture zone, with a mesh edge size set to 0.4 mm. In the rest of the geometry, a coarse meshing is utilized, whose edge size is 2 mm.

### 3.4. Material plasticity model

The tested material is AISI 1045. It is a medium carbon steel containing around 0.45% carbon, known for its good strength, wear resistance, and toughness. The material plasticity is described by the Johnson–Cook model as shown in Eq. (13). The present work is a part from a global study on damage modeling of AISI 1045 for the use in metal forming processes. Johnson–Cook material modeling for both plasticity and damage is adopted in the general study because of its effectiveness in the simulation of forging and machining processes [40]. The equivalent stress is expressed in Eq. (8) as the product of three functions, from left to right: strain hardening, strain rate strengthening, and temperature effect:

$$\sigma_{eq} = \left(A + B\varepsilon_p^n\right)\left(1 + C\ln\left(\frac{\dot{\varepsilon}}{\dot{\varepsilon}_0}\right)\right)\left(1 - \left(\frac{T - T_0}{T_m - T_0}\right)^m\right) \tag{13}$$

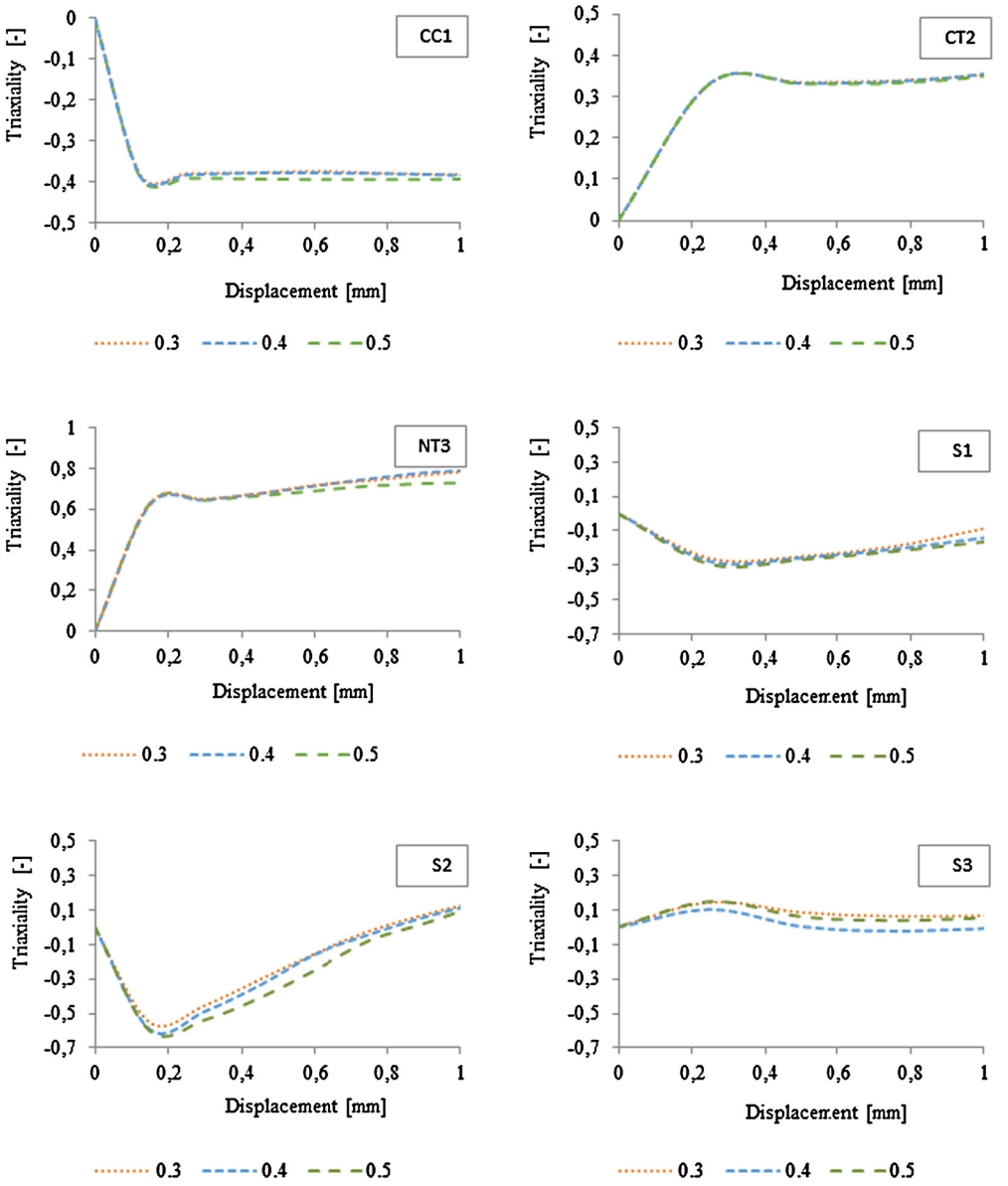


**Fig. 3.** Evolution of the simulated triaxiality using the mesh sizes 0.3, 0.4, and 0.5 mm in the rupture zone of the specimens: CC1, CT2, NT3, S1, S2, and S3.

**Table 1**
Constants of the Johnson–Cook plasticity model of AISI 1045 [41].

| $A$ [MPa] | $B$ [MPa] | $n$ | $C$ | $\dot{\varepsilon}_0$ [$s^{-1}$] | $m$ | $T_m$ [C°] | $T_0$ [C°] |
|---|---|---|---|---|---|---|---|
| 553 | 600 | 0.234 | 0.0134 | 1 | 1 | 1480 | 20 |

where $\varepsilon_p$ is the equivalent plastic strain, $\dot{\varepsilon}$ is the strain rate; $\dot{\varepsilon}_0$ is the reference strain rate (1 $s^{-1}$), $T$ is the temperature, $T_0$ is the reference temperature, and $T_m$ is the melting temperature. The material constants $A$, $B$, $n$, $C$, and $m$ are respectively the yield stress, the strain-hardening coefficient, the strain-hardening exponent, the strain-rate-dependence coefficient, and the temperature-dependence coefficient. These constants were obtained from [41] and are presented in Table 1. Many authors have utilized this set of constants in finite-element simulations of cutting [42–44].

In this paper, the effects of strain rate and temperature are not studied. Therefore, the respective parenthesis terms in Eq. (8) are set to one, taking a constant strain rate $\dot{\varepsilon} = \dot{\varepsilon}_0 = 1$ $s^{-1}$ and a temperature dependence coefficient $m = 0$. Eq. (8) is modified as follows:

$$\sigma_{eq} = 553 + 600(\varepsilon_p)^{0.234} \tag{14}$$

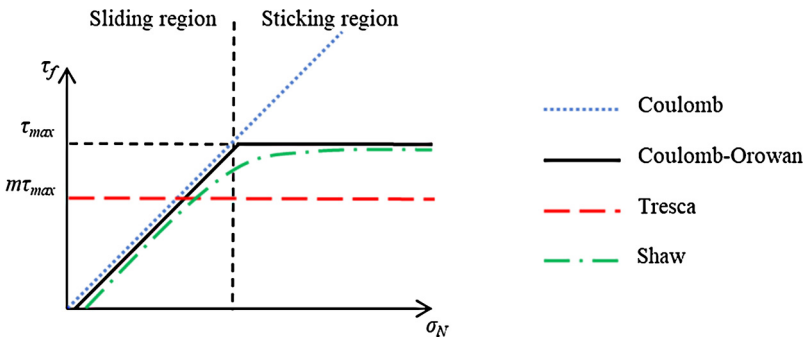


**Fig. 4.** Friction models for the contact between the die and the specimen.

### 3.5. Friction model

The modeling of the friction condition is an important factor in compression tests, which influences the computed geometry and loads. In the realistic characterization tests, friction between specimen and die should be reduced with special techniques, and then experimentally determined with ring tests [45]. The most common friction model is Coulomb friction (Eq. (9)) that assumes the proportionality of the friction shear stress $\tau_f$ to the normal contact stress $\sigma_N$ with the constant coefficient $\mu_C$.

$$\tau_f = \mu_C \cdot \sigma_N \tag{15}$$

In metal forming processes where high contact pressure is induced between the tool and the work piece, the Coulomb friction is physically limited by the material shear stress $\tau_{max}$ [46]. The combined Coulomb–Orowan friction model takes into account both of the above-described contact phenomena and is very popular in bulk metal forming modeling because of its simplicity and convenience.

$$\tau_f = \mathrm{Min}(\mu_C \sigma_N, \tau_{max}) \tag{16}$$

The maximal shear stress $\tau_{max}$ is calculated from the tensile yield stress $\sigma_y$, as the von Mises theory predicts,

$$\tau_{max} = \frac{\sigma_y}{\sqrt{3}} \tag{17}$$

Another known model is Tresca's or constant shear friction model. It is utilized when contact pressure is very high and the sliding friction is neglected. In this case, the friction shear is proportional to the maximal shear stress with the coefficient $m$, which ranges between zero and one:

$$\tau_f = m\frac{\sigma_y}{\sqrt{3}} \tag{18}$$

Shaw has developed the combined friction with a continuous transition between sliding and sticking friction [47],

$$\tau_f = \alpha \tau_{max} \tag{19}$$

where $\alpha$ is the ratio between the effective contact surface and the whole contact surface. Many studies have proposed a mathematical formulation of this ratio [48]. The friction coefficient and friction factor have to satisfy the relationship $\mu_C < 0.577$ m when von Mises' yield criterion is adopted [49].

The combination of Coulomb–Tresca friction (Eq. (9)) has been proven to be effective for bulk metal forming simulations [49]. Fig. 4 illustrates the most known friction models.

$$\tau_f = \mathrm{Min}\left(\mu_C \sigma_N, m\frac{\sigma_y}{\sqrt{3}}\right) \tag{20}$$

This combined Coulomb–Tresca friction model was applied in the current work, assuming a Coulomb factor $\mu_C = 0.1$ and Tresca friction factor $m = 0.45$. the choice of the coefficients is based on previous studies on AISI 1045 in dry friction condition [50,51]. Equation (20) can be rewritten as follows:

$$\tau_f = \begin{cases} 0.1\sigma_N & \text{if } 0.1\sigma_N < 143.67 \text{ MPa} \\ \frac{0.45}{\sqrt{3}} 553 & \text{if } 0.1\sigma_N \geq 143.67 \text{ MPa} \end{cases} \tag{21}$$

Fig. 5 shows the zones where friction was modeled between the tool and the specimen. For the compression test (a), the friction was applied on the upper and lower surfaces ($S_1$) of the cylindrical piece. Two geometries were used in the

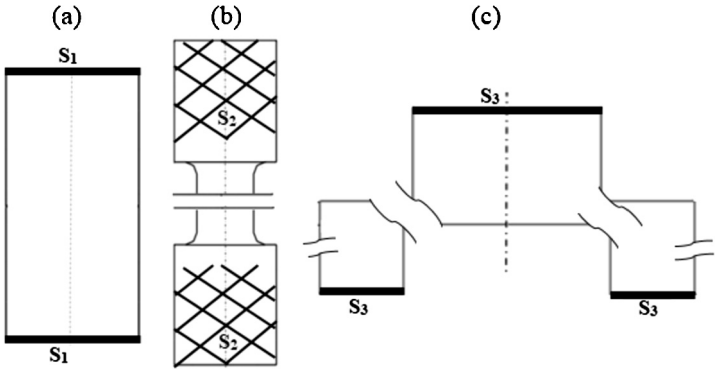


**Fig. 5.** Friction zones in the different specimens.

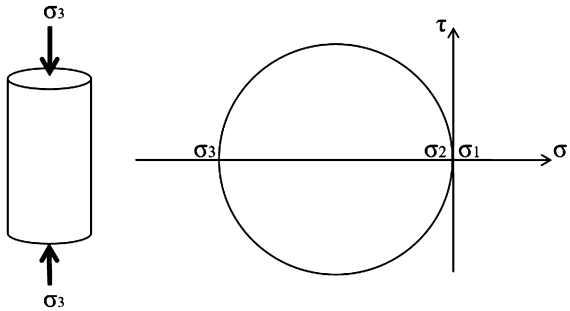


**Fig. 6.** Illustration of the state of uniaxial compression stress.

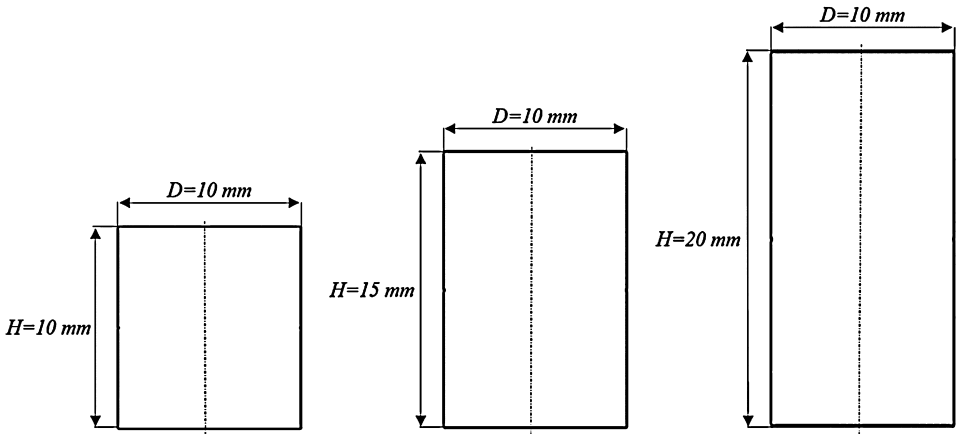


**Fig. 7.** Geometries of the compression test specimens: CC1, CC2, and CC3.

traction test (b): smooth and notched cylindrical specimens. Friction was neglected in traction tests since the ends ($S_2$) were assumed to be fixed with two jaws. In the last test (c), the friction was applied on the upper and lower surfaces ($S_3$) of the specimen.

## 4. Characterization tests modeling

### *4.1. Cylinder compression tests*

Upsetting test corresponds to loading condition with $\sigma_1 = \sigma_2 = 0$ and $\sigma_3 < 0$ in the center of the specimen (Fig. 6). This leads to $\eta = -1/3$ and $\mu = 1$ (Eqs. (4)–(5)) under a frictionless state. According to [52], these values are nearly met when the ratio $D/H$ is very small (where $D$ is the initial diameter and $H$ is the initial height). However, in this case, a risk of buckling of the specimen is encountered.

Three cylinder geometries having the same initial diameter are considered (Fig. 7). The initial diameter-to-height ratio takes the following values: 1, 0.6667, and 0.5, respectively, for specimens CC1, CC2, and CC3.

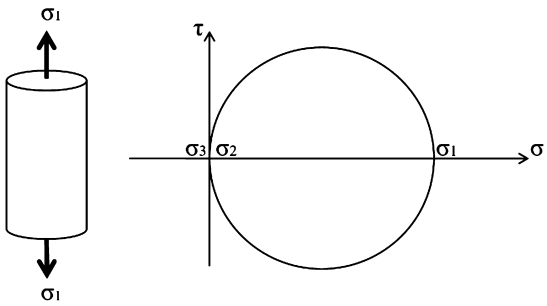


**Fig. 8.** Illustration of the uniaxial tension stress state.

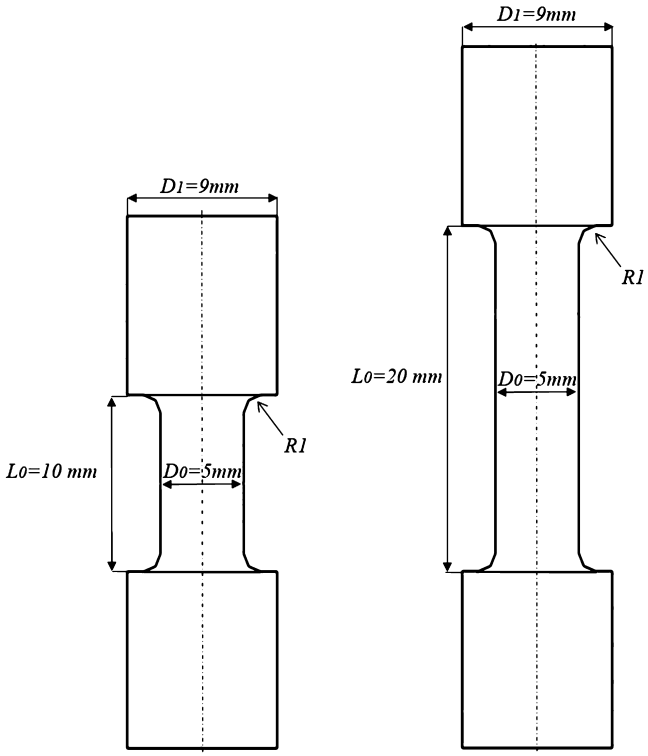


**Fig. 9.** Geometries of smooth bar specimens: CT1 and CT2.

### 4.2. Traction tests on smooth round bars

In the general case of uniaxial tension, the principal stresses in the center of the specimen are as follows: $\sigma_2 = \sigma_3 = 0$ and $\sigma_1 > 0$ (Fig. 8). Consequently, $\eta = 1/3$ and $\mu = -1$ (Eqs. (4)–(5)).

Two geometries are modeled with the same initial diameter of the reduced section ($D_0$) and different initial distances between shoulders ($L_0$) (Fig. 9).

The selected $L_0/D_0$ ratios are 2 and 4, respectively, for CT1 and CT2.

### 4.3. Tests on notched round bars

The notch has to increase the triaxiality in the minimal cross-section zone of the specimen [53]. The initial triaxiality in the center of the geometry can be written as a function of the radius of the minimal cross section (a) and the notch radius in the notched round bar ($R$) [6,54].

$$\eta = \frac{1}{3} + \ln\left(1 + \frac{a}{2R}\right) \tag{22}$$

In this section, four cylindrical notched specimens having the same minimal cross-section diameter ($D_0$) and maximal diameter ($D_1$) are compared (Fig. 10).

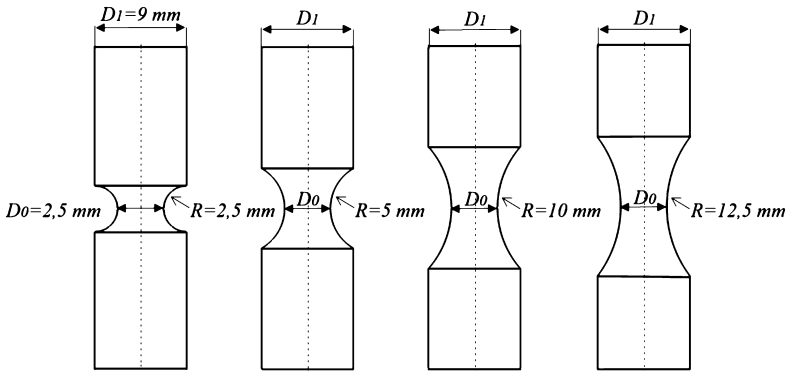


**Fig. 10.** Geometries of the notched bar specimens: NT1, NT2, NT3, and NT4.

**Table 2**
Theoretical values of triaxiality in the notched round specimens.

| Specimen | NT1 | NT2 | NT3 | NT4 |
|---|---|---|---|---|
| $R$ | 2.5 | 5 | 10 | 12.5 |
| $\eta$ | 1.017 | 0.732 | 0.552 | 0.512 |

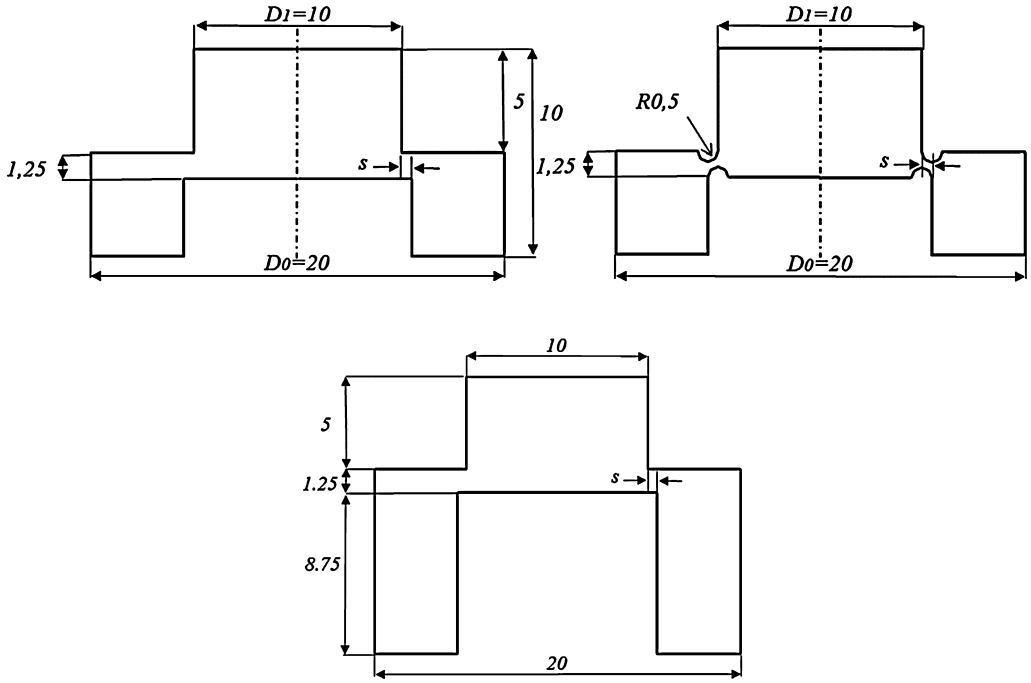


**Fig. 11.** Geometries of the shear specimens: S1, S2, and S3.

The theoretical values of triaxiality according to Eq. (22) are listed in Table 2. The Lode parameter takes the value $\mu = -1$, since the stress state is an axisymmetric tension [55].

### 4.4. Shear tests

Pure shear loading is characterized by $\sigma_3 = -\sigma_1$ and $\sigma_2 = 0$ in the critical zone where rupture occurs. Consequently, $\eta = \mu = 0$ (Eqs. (4), (5)). Three geometries are compared (Fig. 11).

In these specimens, the shearing condition in bulk metal is reproduced in a small area whose height is 1.25 mm and width $s = 0.5$ mm in all types of specimen. Specimens S1 and S2 are axisymmetric, unlike specimen S3. A combined friction model is applied between the specimens and the dies.

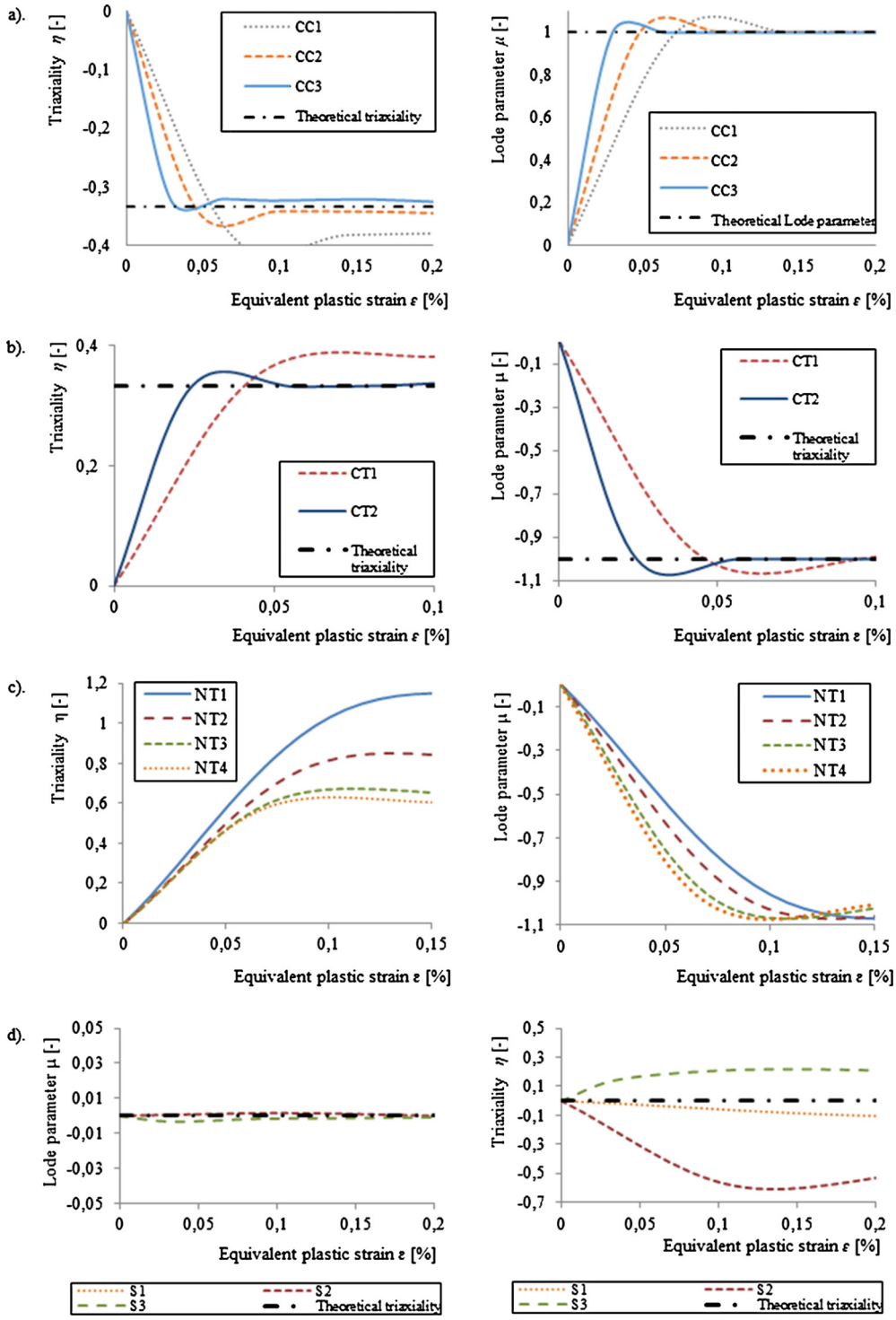


**Fig. 12.** Comparison of the evolution of triaxiality and the Lode parameter in simulated: a) upsetting tests, b) traction on smooth round bars, c) traction on notched bars, d) shear tests.

## 5. Results and discussion

The simulated stress state variables in the critical element are represented and analyzed in Fig. 12. In all tests, the stress state observation is carried out until a strain of 0.2. This choice is based on the study of Moćko [56]. He has calculated the true stress–true strain curve from tensile tests on cylindrical specimens. The material failure occurred at a true strain of 0.2.

**Table 3**
Theoretical and computed values of triaxiality in the notched round specimens.

| Specimen | NT1 | NT2 | NT3 | NT4 |
|---|---|---|---|---|
| Theoretical triaxiality | 1.017 | 0.732 | 0.552 | 0.512 |
| Computed triaxiality | 1.080 | 0.790 | 0.623 | 0.583 |
| Deviation | 6% | 8% | 13% | 14% |

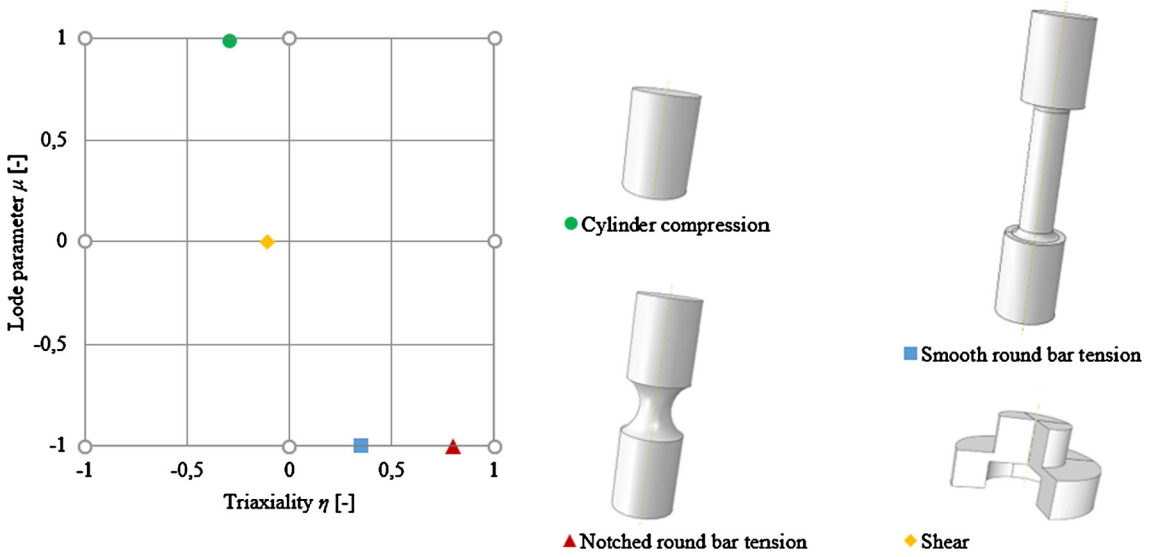


**Fig. 13.** Positioning of the selected bulk characterization of test specimens in the triaxiality–Lode parameter space.

In the upsetting tests, the triaxiality of specimen CC3 is relatively more stable during loading and converges to $-0.287$, which approaches the analytical value $-1/3$. The Lode parameter converges to the theoretical value 1 for all specimens. In general, the deviation from the theoretical values of $\eta$ and $\mu$ decreases with decreasing the $D/H$ ratio of the upsetting specimens. Furthermore, specimen CC3 has the most stable stress state through the deformation.

We can see that the triaxiality of the central element of smooth traction specimen CT2 converges to the theoretical value 0.33 from a strain of 0.055. The Lode parameter calculated in the central element of this specimen converges to the theoretical value $-1$ at the strain 0.055 too. We conclude that the values of $\eta$ and $\mu$ are closer to the theoretical values when the ratio $L_0/D_0$ is larger. Consequently, specimen CT2 is more appropriate for characterization tests. In Table 3, theoretical and simulated convergence triaxiality values in the critical elements of notched specimens are compared. The deviation in percentage is relatively small for specimens NT1 and NT2.

In the case of specimen NT2, the curve of triaxiality is relatively stable compared to the case of specimens NT3 and NT4. It attains the theoretical value $-1$ before specimen NT1.

The evolutions of the Lode parameter of specimens S1 and S2 are very close to the theoretical value 0. Otherwise, the evolution of triaxiality along the deformation in shear tests shows that the most stable curve that approaches the theoretical value 0 is to see in the case of specimen S1. Consequently, specimen S1 will be retained.

To recapitulate, four specimens were selected for the characterization of AISI 1045 steel: CC3, CT2, NT2 and S1. To have an idea of the diversification of stress states, the convergence values of $\eta$ and $\mu$ of each specimen were plotted in the triaxiality–Lode parameter space (Fig. 13).

The simulated characterization tests cover a large range of triaxiality and Lode parameter thanks to the various geometries. Compression, pure shear and tension stress states were obtained with the typical Lode parameter values 1, 0, and $-1$, respectively. For tension stress state, two variants were realized, having low and high triaxiality. The first and the third quadrant in Fig. 13, which represent the domains of equibiaxial tension and equibiaxial compression, respectively, are empty because both of these stress states are not considered in this research. Stress states with low Lode parameter values ($-0.5 < \mu < 0.5$) apart from pure shear are not achieved. In the characterization of metal sheets, these stress states are attained thanks to butterfly specimens [57]. In characterization tests of bulk metal, a Lode parameter of 0.5 can be realized with the combination of tension–torsion stresses on cylindrical specimens [58]. Plane-strain tension and compression cases, which are realizable with flat specimens, have not been studied here either because this study focuses on bulk specimens.

## 6. Conclusion

Ductility modeling is important to predict workability and failure in many bulk metalworking processes. Precise bulk material damage modeling requires characterization tests on bulk specimens. Compared to the abundant studies on the characterization of metal sheets, characteristic tests of bulk metals have to be developed to reproduce all of the possible stress states in bulk metalworking processes. The different stress states are attainable with varying the geometry and the loading in the characterization tests.

In this article, the influence of geometry on the stress state has been proven and numerically analyzed. Simulations of four characterization test types were carried out: upsetting tests, traction on smooth round bars, traction on notched round bars and shear tests. Since damage mechanisms are dependent on all three stress invariants, the analysis of the stress state is based on the observation of the evolution of the computed stress triaxiality and the Lode parameter. The consideration of both of these variables is necessary to envelop various stress states. In every test category, the most representative specimen of the respective stress state was depicted based on the stability through the deformation and closeness to the analytical values of both triaxiality and Lode parameter.

## References

[1] M.B. Silva, K. Isik, A.E. Tekkaya, P.A.F. Martins, Fracture loci in sheet metal forming: a review, Acta Metall. Sin. Engl. Lett. 28 (2015) 1415–1425, https://doi.org/10.1007/s40195-015-0341-6.
[2] F. Rastellini, G. Socorro, A. Forgas, E. Onate, A triaxial failure diagram to predict the forming limit of 3D sheet metal parts subjected to multiaxial stresses, J. Phys. Conf. Ser. 734 (2016) 032020, https://doi.org/10.1088/1742-6596/734/3/032020.
[3] H. Hentati, M. Dhahri, F. Dammak, A phase-field model of quasistatic and dynamic brittle fracture using staggered algorithm, J. Mech. Mater. Struct. 11 (3) (2016) 309–327, https://doi.org/10.2140/jomms.2016.11.309.
[4] I. Barsoum, J. Faleskog, Rupture mechanisms in combined tension and shear-experiments, Int. J. Solids Struct. 44 (2007) 1768–1786, https://doi.org/10.1016/j.ijsolstr.2006.09.031.
[5] C.M.A. Silva, L.M. Alves, C.V. Nielsen, A.G. Atkins, P.A.F. Martins, Failure by fracture in bulk metal forming, J. Mater. Process. Technol. 215 (2015) 287–298, https://doi.org/10.1016/j.jmatprotec.2014.08.023.
[6] P.W. Bridgman, Studies in large plastic flow and fracture: with special emphasis on the effects of hydrostatic pressure, http://books.google.com/books?id=vbU8AAAAIAAJ, 1964.
[7] V. Vujovic, A.H. Shabaik, A new workability criterion for ductile metals, J. Eng. Mater. Technol. 108 (1986) 245, https://doi.org/10.1115/1.3225876.
[8] E. Ghassemali, X. Song, M. Zarinejad, D. Atsushi, M.J. Tan, Bulk metal forming processes in manufacturing, in: A. Nee (Ed.), Handbook of Manufacturing Engineering and Technology, Springer, London, 2013, pp. 1–50.
[9] P. Christiansen, C. Nielsen, N. Bay, P. Martins, Internal shear cracking in bulk metal forming, Proc. Inst. Mech. Eng. Part J. Mater. Des. Appl. 233 (4) (2019) 146442071668159, https://doi.org/10.1177/1464420716681592.
[10] J.R. Rice, D.M. Tracey, On the ductile enlargement of voids in triaxial stress fields, J. Mech. Phys. Solids 17 (1969) 201–217, https://doi.org/10.1016/0022-5096(69)90033-7.
[11] Y. Bao, T. Wierzbicki, On fracture locus in the equivalent strain and stress triaxiality space, Int. J. Mech. Sci. 46 (2004) 81–98, https://doi.org/10.1016/j.ijmecsci.2004.02.006.
[12] G. Mirone, Role of stress triaxiality in elastoplastic characterization and ductile failure prediction, Eng. Fract. Mech. 74 (2007) 1203–1221, https://doi.org/10.1016/j.engfracmech.2006.08.002.
[13] M. Oyane, T. Sato, K. Okimoto, S. Shima, Criteria for ductile fracture and their applications, J. Mech. Work. Technol. 4 (1980) 65–81, https://doi.org/10.1016/0378-3804(80)90006-6.
[14] L.P. Lei, J. Kim, B.S. Kang, Bursting failure prediction in tube hydroforming processes by using rigid-plastic FEM combined with ductile fracture criterion, Int. J. Mech. Sci. 7 (2002) 1411–1428.
[15] P. Christiansen, J.H. Hattel, N. Bay, K. Lyngby, P.A.F. Martins, Modelling of damage during hot forging of ingots, in: Proc. Conference 5th International Conference on Modelling and Simulation of Metallurgical Processes in Steelmaking, STEELSIM 2013, Ostrava, Czech Republic, September 2013, pp. 10–12.
[16] G.R. Johnson, W.H. Cook, Fracture characteristics of three metals subjected to various strains, strain rates, temperatures and pressures, Eng. Fract. Mech. 21 (1985) 31–48, https://doi.org/10.1016/0013-7944(85)90052-9.
[17] M. Murugesan, D.W. Jung, Johnson–Cook material and failure model parameters estimation of AISI-1045 medium carbon steel for metal forming applications, Materials 12 (2019) 609, https://doi.org/10.3390/ma12040609.
[18] S. Chocron, B. Erice, C.E. Anderson, A new plasticity and failure model for ballistic application, Int. J. Impact Eng. 38 (2011) 755–764, https://doi.org/10.1016/j.ijimpeng.2011.03.006.
[19] H. Hentati, I.B. Naceur, W. Bouzid, A. Maalej, Numerical analysis of damage thermo-mechanical models, Adv. Appl. Math. Mech. 7 (5) (2015) 625–643, https://doi.org/10.4208/aamm.2014.m517.
[20] L.E. Lindgren, A. Svoboda, D. Wedberg, M. Lundblad, Computational simulation of manufacturing processes towards predictive simulations of machining, C. R. Mecanique 344 (2016) 284–295.
[21] Y. Bai, T. Wierzbicki, A new model of metal plasticity and fracture with pressure and Lode dependence, Int. J. Plast. 24 (2008) 1071–1096, https://doi.org/10.1016/j.ijplas.2007.09.004.
[22] Y. Bai, T. Wierzbicki, A comparative study of three groups of ductile fracture loci in the 3D space, Eng. Fract. Mech. 135 (2015) 147–167, https://doi.org/10.1016/j.engfracmech.2014.12.023.
[23] K.S. Zhano, Z.H. Li, Numerical analysis of the stress-strain curve and fracture initiation for ductile material, Eng. Fract. Mech. 49 (1994) 235–241, https://doi.org/10.1016/0013-7944(94)90006-X.
[24] B. Erice, F. Gálvez, A coupled elastoplastic-damage constitutive model with Lode angle dependent failure criterion, Int. J. Solids Struct. 51 (2014) 93–110, https://doi.org/10.1016/j.ijsolstr.2013.09.015.
[25] P.A.F. Martins, N. Bay, A.E. Tekkaya, A.G. Atkins, Characterization of fracture loci in metal forming, Int. J. Mech. Sci. 83 (2014) 112–123, https://doi.org/10.1016/j.ijmecsci.2014.04.003.
[26] L.W. Meyer, T. Halle, Shear strength and shear failure, overview of testing and behavior of ductile metals, Mech. Time-Depend. Mater. 15 (2011) 327–340, https://doi.org/10.1007/s11043-010-9113-x.
[27] G.R. Johnson, W.H. Cook, A constitutive model and data for metals subjected to large strains, high strain rates and high temperatures, in: Proc. Seventh International Symposium on Ballistics, The Hague, the Netherlands, 19–21 April, 1983, http://wbldb.lievers.net/10134084.html. (Accessed 23 March 2019).

[28] H. Ijaz, M. Zain-ul-abdein, W. Saleem, M. Asad, T. Mabrouki, Modified Johnson–Cook plasticity model with damage evolution: application to turning simulation of 2XXX aluminium alloy, J. Mech. 33 (2017) 777–788, https://doi.org/10.1017/jmech.2017.11.
[29] M. Rodriguez-Millan, D. Garcia-Gonzalez, A. Rusinek, A. Arias, Influence of stress state on the mechanical impact and deformation behaviors of aluminum alloys, Metals 8 (2018) 520, https://doi.org/10.3390/met8070520.
[30] M. Alebooyeh, H.R. Baharvandi, C. Aghanajafi, Two-dimensional FE simulation of impact loading on alumina matrix nanocomposite reinforced by Dyneema® HB25 laminates, J. Mech. 33 (2017) 1–11, https://doi.org/10.1017/jmech.2016.26.
[31] H. Autenrieth, V. Schulze, N. Herzig, L.W. Meyer, Ductile failure model for the description of AISI 1045 behavior under different loading conditions, Mech. Time-Depend. Mater. 13 (2009) 215–231, https://doi.org/10.1007/s11043-009-9084-y.
[32] S.P.F.C. Jaspers, J.H. Dautzenberg, Material behaviour in conditions similar to metal cutting: flow stress in the primary shear zone, J. Mater. Process. Technol. 122 (2002) 322–330, https://doi.org/10.1016/S0924-0136(01)01228-6.
[33] W. Lode, Versuche über den Einfluß der mittleren Hauptspannung auf das Fließen der Metalle Eisen, Kupfer und Nickel, Z. Phys. 36 (1926) 913–939, https://doi.org/10.1007/BF01400222.
[34] J.P. Bardet, Lode dependences for isotropic pressure-sensitive elastoplastic materials, J. Appl. Mech. Trans. ASME 57 (1990) 498–506.
[35] C.F. Guzmán, About the Lode Angle Influence in Ductile Fracture, Technical Report, University of Liège, Belgium, 2013.
[36] K. Danas, P. Ponte Castañeda, Influence of the Lode parameter and the stress triaxiality on the failure of elasto-plastic porous materials, Int. J. Solids Struct. 49 (2012) 1325–1342, https://doi.org/10.1016/j.ijsolstr.2012.02.006.
[37] S. Moakhar, H. Hentati, M. Barkallah, J. Louati, C. Bonk, B.A. Behrens, M. Haddar, Evaluation of AW-6082 aluminium bar shearing simulation, in: Lecture Note in Mechanical Engineering, ISBN 978-3-030-24246-6, 2019.
[38] C.L. Hu, L.Q. Chen, Z. Zhao, J.W. Li, Z.M. Li, Study on the pre-shearing cropping process of steel bars, Int. J. Adv. Manuf. Technol. 97 (2018) 783–793, https://doi.org/10.1007/s00170-018-1979-9.
[39] L.F. Menezes, J.V. Fernandes, D.M. Rodrigues, Numerical simulation of tensile tests of prestrained sheets, Mater. Sci. Eng., A. 264 (1999) 130–138, https://doi.org/10.1016/S0921-5093(98)01104-6.
[40] A. Hor, F. Morel, J.L. Lebrun, G. Germain, Modelling, identification and application of phenomenological constitutive laws over a large strain rate and temperature range, Mech. Mater. 64 (2013) 91–110, https://doi.org/10.1016/j.mechmat.2013.05.002.
[41] S.P.F.C. Jaspers, J.H. Dautzenberg, Material behaviour in metal cutting: strains, strain rates and temperatures in chip formation, J. Mater. Process. Technol. 121 (2002) 123–135, https://doi.org/10.1016/S0924-0136(01)01227-4.
[42] C.Z. Duan, H.Y. Yu, Y.J. Cai, Y.Y. Li, Finite element simulation and experiment of chip formation during high speed cutting of hardened steel, Appl. Mech. Mater. 29–32 (2010) 1838–1843, https://doi.org/10.4028/www.scientific.net/AMM.29-32.1838.
[43] M.N.A. Nasr, Effects of sequential cuts on residual stresses when orthogonal cutting steel AISI 1045, Proc. CIRP 31 (2015) 118–123, https://doi.org/10.1016/j.procir.2015.03.032.
[44] M.N.A. Nasr, M.M.A. Ammar, An evaluation of different damage models when simulating the cutting process using FEM, Proc. CIRP 58 (2017) 134–139, https://doi.org/10.1016/j.procir.2017.03.202.
[45] P. Christiansen, C.V. Nielsen, P.A.F. Martins, N. Bay, Predicting the onset of cracks in bulk metal forming by ductile damage criteria, Proc. Eng. 207 (2017) 2048–2053, https://doi.org/10.1016/j.proeng.2017.10.1106.
[46] E. Orowan, The calculation of roll pressure in hot and cold flat rolling, Proc. Inst. Mech. Eng. 150 (1943) 140–167, https://doi.org/10.1243/PIME_PROC_1943_150_025_02.
[47] M.C. Shaw, The role of friction in deformation processing, Wear 6 (1963) 140–158, https://doi.org/10.1016/0043-1648(63)90126-1.
[48] F. Klocke, Manufacturing Processes 4: Forming, Springer Science & Business Media, 2014.
[49] D.W. Zhang, H. Ou, Relationship between friction parameters in a Coulomb–Tresca friction model for bulk metal forming, Tribol. Int. 95 (2016) 13–18, https://doi.org/10.1016/j.triboint.2015.10.030.
[50] R. Chandramouli, Thermal effects and friction in forming, NPTEL web course – mechanical engineering – forming, n.d.: p. 10, https://nptel.ac.in/content/storage2/courses/112106153/Module%2010/Lecture%204/Module_10_Lecture_4_Thermaleffects-friction-Quiz_Key.pdf.
[51] D.M.R. Cecil, A. Rajadurai, Friction evaluation in metal forming using upsetting test, J. Inst. Eng. India Part PR Prod. Eng. Div. 90 (2010) 28–32.
[52] K. Karpanan, W. Thomas, Influence of lode angle on the ASME local strain failure criterion, in: Proceedings of the ASME 2018 Pressure Vessels and Piping Conference, PVP2018, Vancouver, Canada, 17–21 June, 2016.
[53] L. Driemeier, M. Brünig, G. Micheli, M. Alves, Experiments on stress-triaxiality dependence of material behavior of aluminum alloys, Mech. Mater. 42 (2010) 207–217, https://doi.org/10.1016/j.mechmat.2009.11.012.
[54] Y. Bai, X. Teng, T. Wierzbicki, On the application of stress triaxiality formula for plane strain fracture testing, J. Eng. Mater. Technol. 131 (2009) 021002, https://doi.org/10.1115/1.3078390.
[55] I. Barsoum, J. Faleskog, S. Pingle, The influence of the lode parameter on ductile failure strain in steel, Proc. Eng. 10 (2011) 69–75, https://doi.org/10.1016/j.proeng.2011.04.014.
[56] W. Moćko, Effects of cumulative fatigue damage under tensional cyclic loading on the constitutive relation of AISI 1045 steel, in: Proc. Fourth International Conference on Nonlinear Dynamics, Sevastopol, Ukraine, 19–22 June, 2013, http://www.ippt.pan.pl/Repository/o1962.pdf. (Accessed 15 March 2019).
[57] M. Basaran, S.D. Wölkerling, M. Feucht, F. Neukamm, D. Weichert, An extension of the GISSMO damage model based on lode angle dependence, in: Proc. 9th LS-DYNA Forum, Stuttgart, Germany, 2010, pp. 3–17.
[58] E. Bombasaro, Effect of the Lode Angle Parameter on the Behavior of Aluminum, Master Thesis, University of Houston, Cullen College of Engineering, Houston, TX, USA, 2014.